Common behavioral mechanisms underlie *C. elegans* aggregation and swarming

S Serena Ding[1,2]*, Linus J Schumacher[3,4]*, Avelino Javer[1,5,6], Robert G Endres[3], André EX Brown[1,2]

[1]MRC London Institute of Medical Sciences, London, UK; [2]Instititue of Clinical Sciences, Imperial College London, London, UK; [3]Department of Life Sciences, Imperial College London, London, UK; [4]Present address: MRC Centre for Regenerative Medicine, University of Edinburgh, Edinburgh, UK; [5]Present address: Institute of Biomedical Engineering, University of Oxford, Oxford, UK; [6]Present address: Data Science Institute, University of Oxford, Oxford, UK

*these authors contributed equally
correspondence to: r.endres@imperial.ac.uk or andre.brown@imperial.ac.uk

Abstract

In complex biological systems, simple individual-level behavioral rules can give rise to emergent group-level behavior. While such collective behavior has been well studied in cells and larger organisms, the mesoscopic scale is less understood, as it is unclear what physical processes matter *a priori*. Here, we investigate collective feeding in the roundworm *C. elegans* at this intermediate scale, and use quantitative phenotyping and agent-based modeling to identify behavioral rules underlying both aggregation and a novel swarming phenotype which we report for the first time. Using fluorescent multi-worm tracking, we quantify aggregation behavior in terms of individual dynamics and population-level statistics. Based on our quantification, we use agent-based simulations and approximate Bayesian inference to identify two key behavioral rules that give rise to aggregation, namely cluster-edge reversals and density-dependent switch between crawling speeds. While this leads to aggregation in simulations, extending the model with a mid-range taxis interaction improves quantitative agreement with aggregation measured in experiments. Additionally, using our extended model we suggest that dynamic swarming is driven by local food depletion and otherwise employs the same behavioral mechanisms as the initial aggregate formation. Our results suggest that mesoscopic *C. elegans* uses mechanisms familiar from microscopic systems for aggregation, but implemented via more complex behaviors, which is characteristic of macroscopic organisms.

Keywords: emergent behavior, collective behavior, behavioral quantification, agent-based modeling, *C. elegans*, aggregation, animal tracking, swarming

Introduction

Collective behavior has been widely studied in living and non-living systems. While very different in their details, shared principles have begun to emerge, such as the importance of alignment for flocking behavior in both theoretical models and birds (Bialek et al., 2012; Pearce, Miller, Rowlands, & Turner, 2014; Reynolds, 1987). Until now, the study of collective behavior has mainly focused on cells and active particles at the microscale, controlled by molecule diffusion and direct contact between cells or particles (Köhler, Schaller, & Bausch, 2011; Palo, Yi, & Endres, 2017; Peruani et al., 2012; Starruss et al., 2012), and on animals at the macroscale, aided by long-range visual cues (Bialek et al., 2012; Katz, Tunstrøm, Ioannou, Huepe, & Couzin, 2011; Pearce et al., 2014). Collective behavior at the intermediate mesoscale is less well-studied, as it is unclear what processes to include *a priori*. At the mesoscale, sensory cues and motility may still be limited by the physics of diffusion and low Reynolds numbers, respectively, yet the inclusion of nervous systems allows for increased signal processing and a greater behavioral repertoire. So do the rules governing collective behavior at this intermediate scale resemble those at the micro- or the macro-scale, some mixture of both, or are new principles required?

Dissecting the mechanisms of *C. elegans* social phenomena can contribute to bridging the scale gap in understanding collective behavior. Some strains of this 1 mm-long roundworm are known to aggregate into groups on food patches (de Bono & Bargmann 1998); here we also report a novel dynamic swarming phenotype that occurs over longer time periods. *C. elegans* represents an intermediate scale not only in physical size but also in behavioral complexity - crawling with negligible inertia, limited to touch and chemical sensing, yet possessing a compact nervous system with only 302 neurons (White, Southgate, Thomson, & Brenner, 1986). Wild *C. elegans* form clusters on food at ambient oxygen concentrations, as do loss-of-function neuropeptide receptor 1 (*npr-1*) mutants. The laboratory reference strain N2, on the other hand, has a gain-of-function mutation in the *npr-1* gene that suppresses aggregation (de Bono & Bargmann 1998), rendering N2 animals solitary feeders. Thus, a small genotypic difference (just two base pairs in one gene for the *npr-1* mutant) has a big effect on the population-level behavioral phenotype. While previous research on collective feeding has primarily qualitatively characterized behavioral components associated with aggregation, including reversals in crawling direction and changes in speed (Busch et al., 2012; Cheung, Cohen, Rogers, Albayram, & de Bono, 2005; Jang et al., 2017; Rogers, Persson, Cheung, & de Bono, 2006), a quantitative mechanistic understanding of aggregation and dynamic swarming in *C. elegans* is still missing.

In this paper, we initially focus on gaining a mechanistic understanding of steady-state aggregation; we hypothesize it also underlies dynamic swarming based on experimental observations. We use fluorescence imaging followed by multi-worm tracking to examine individual behavior inside aggregates for the first time. We present new and systematic quantification of the aggregation behavior in hyper-social *npr-1(ad609lf)* mutants (henceforth referred to as *npr-1* mutants) and hypo-social N2 worms. Next, we draw on the concept of motility-induced phase transitions to explain aggregation as an emergent phenomenon by modulating only a few biophysical parameters. Unlike aggregation driven by attractive forces, in motility-induced phase transitions individuals can also aggregate simply due to their active movement and non-attractive interactions, such as volume exclusion (avoidance of direct overlap) (Redner, Baskaran, et al. 2013). For instance, this concept has contributed understanding to the aggregation of rod-shaped *Myxococcus xanthus* bacteria, which, similar to *C. elegans*, also exhibit reversals during aggregation (Peruani et al., 2012; Starruss et al., 2012). We build an agent-based

phenomenological model of simplified worm motility and interactions. By mapping out a phase diagram of behavioral phenotypes, we show modulating cluster-edge reversals and density-dependent switch between crawling speeds produce various aggregation phenotypes. We further discuss how adding a medium-range taxis interaction further improves the match of strain-specific clustering details to those measured in experiments. Last but not least, our extended model shows that the same behavioral rules, when combined with food depletion, give rise to swarming over time. Together, these developments provide a powerful framework for unraveling the mechanisms underlying collective behavior in *C. elegans* and other systems.

Results

Dynamic swarming occurs in social worms at long time scales

Aggregation has previously been depicted as a semi-steady state phenomenon, with individual worms moving in and out of clusters. Here we report a novel dynamic phenotype, which we call swarming, that is only noticeable at longer time scales (hours). A high number of *npr-1* mutants not only aggregate into dense clusters, but also swarm across the bacteria lawn over time (Figure 1A). Despite being visually striking, this phenomenon may have been missed before due to shorter experimental durations (minutes) with fewer worms in previous work.

Dynamic swarming occurs with just 40 *npr-1* mutants (Figure 1B, top row), making it experimentally feasible to study. It is not observed with solitary N2 worms (Figure 1B, bottom row). Under our experimental conditions at atmospheric oxygen levels, usually a single *npr-1* aggregate forms on the food patch and then moves around the lawn in a persistent but not necessarily directed manner (Figure 1C, left; Supplementary Figure S1A). The onset of this collective movement appears to coincide with local food depletion, and continues until complete food depletion, at which time the cluster disperses. More than one moving cluster may co-exist, and occasionally a cluster may disperse and form elsewhere when it crosses its previous path (Supplementary Figure S1A), presumably due to local food depletion. The observed pattern of *npr-1* cluster motion is reminiscent of a self-avoiding, persistent random walk (i.e. not going back to areas that the worms have previously been where there is no food left). By contrast, after initially forming transient clusters on the lawn, N2 worms move radially outwards with no collective movement (Figure 1C, right).

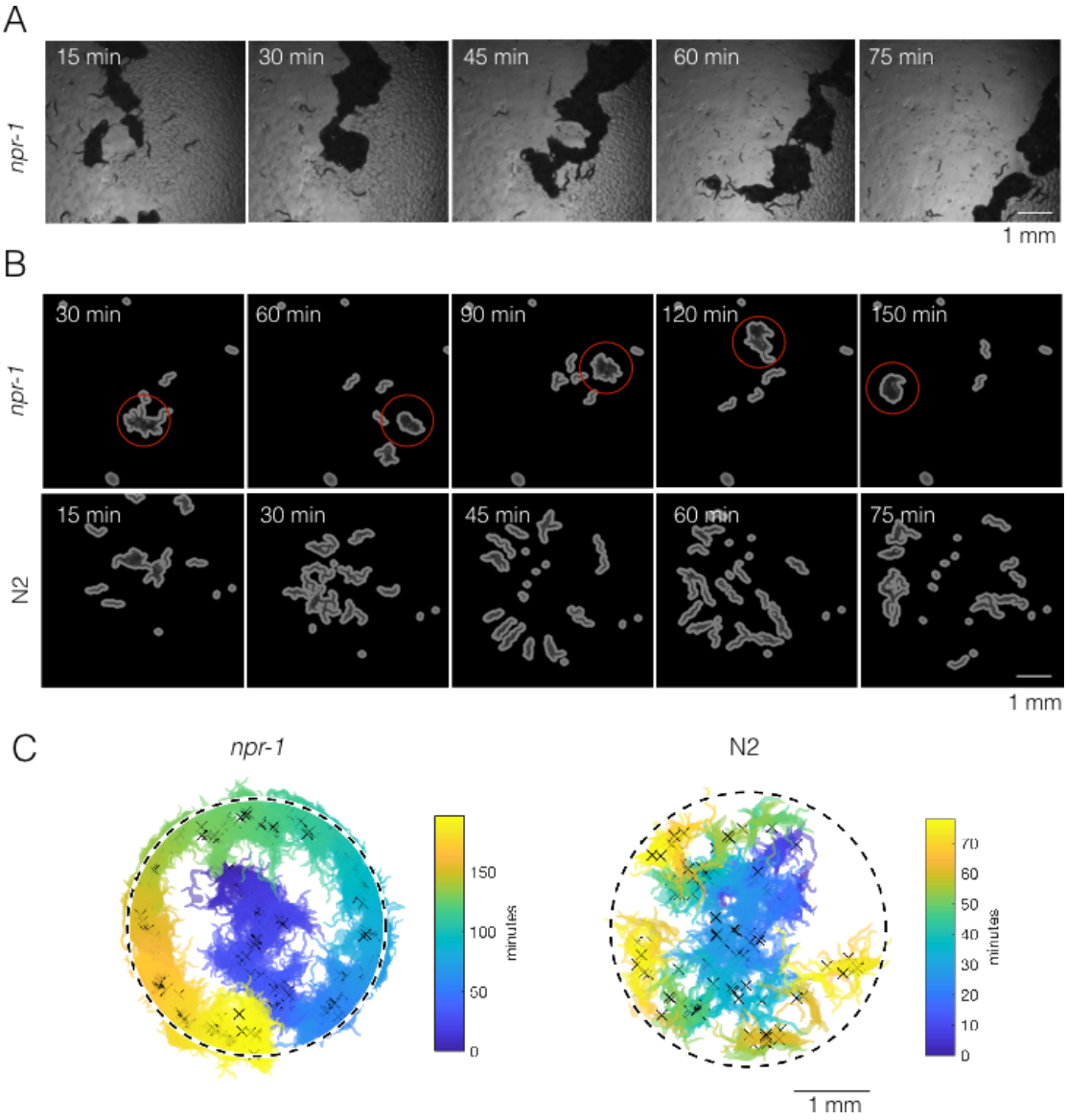

Figure 1. *npr-1* but not N2 worms show swarming behavior over time. A) A few hundred *npr-1* mutant worms form dense clusters that move over time on food. B) Forty *npr-1* mutant worms also cluster and swarm on food (red circles encompass the same cluster over time). The same number of N2 worms do not swarm and disburse after initial transient aggregation. C) Visualization of persistent swarming over time. One frame was sampled every 30 s over the duration of the movies and binary segmentation was applied using an intensity threshold to separate worm pixels from the background. Blob measurements were made using the regionprops function in Matlab and blobs with areas above a threshold value were plotted as clusters to show cluster position over time. The same movies as in (B) were used. Dashed circles show the outer edge of the food patch. Crosses are cluster centroids at each sample frame.

Fluorescence imaging and automated animal tracking allows quantification of dynamics inside and outside of aggregates

Based on our observation that swarming appears to be driven by food depletion, we hypothesize the phenomenon be a dynamic extension of the more steady-state aggregation behavior. Therefore, we elect to initially focus on identifying the mechanisms underlying aggregation.

The presence of aggregates is clear in bright field images, but it is difficult to track individual animals in these strongly overlapping groups for quantitative behavioral analysis. We therefore labeled the pharynx of worms with GFP and used fluorescence imaging in order to minimize overlap between animals, making it possible to track most individuals even when they are inside a dense cluster (Figure 2A). We also labeled a small number of worms (1-3 animals out of 40 per experiment) with an RFP-tagged body wall muscle marker instead of pharynx-GFP. These RFP-labeled worms were recorded on a separate channel during two-color simultaneous imaging (Figure 2B), thus allowing both longer trajectories and the full posture to be obtained in a subset of animals. We wrote a custom module for Tierpsy Tracker to segment light objects on a dark background and to identify the anterior end of the pharynx automatically, in order to extract trajectories and skeletons of multiple worms from our data (Figure 2C).

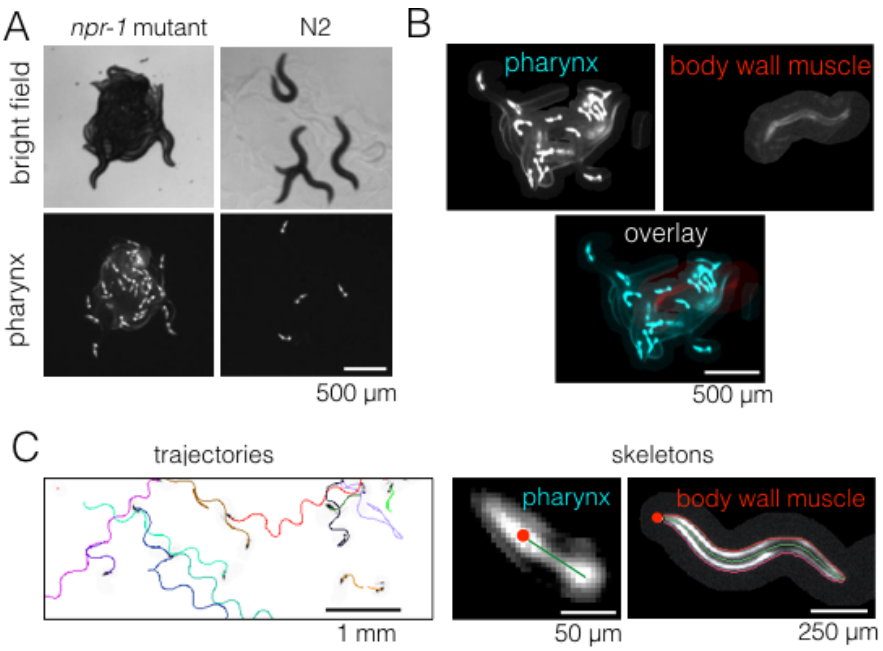

Figure 2. Fluorescent multi-worm tracking. A) *npr-1* mutant and N2 animals exhibit different social behaviors on food, with the former being social (top left) and the latter being solitary (top right). Using a pharynx-GFP label (bottom row), individual animals may be followed inside a cluster. B) In two-color experiments, worms are either labeled with pharynx-GFP (top left) or body wall muscle-RFP (top right). As the two colors are simultaneously acquired on separate channels, the selected few RFP-labeled individuals are readily segmented and may be tracked for a long time, even inside a very dense cluster. C) Tierpsy Tracker software tracks multiple worms simultaneously, generating both centroid trajectories (left, image color inverted for easier visualization; multiple colors show distinct trajectories) and skeletons (middle, pharynx-marked animal; right, body wall muscle-marked animal; red dots denote the head nodes of the skeleton).

Long-range and some short-range interactions are unlikely to drive different aggregation phenotypes

We restricted our search for potential behavioral mechanisms to short-range interactions. Long-range chemotaxis of food can likely be ignored as our experiments were performed on thin, even bacterial lawns. We further excluded any long-range interactions through diffusible pheromones. Although pheromones are important for processes such as mating and dauer formation in *C. elegans* (Srinivasan et al., 2008), it is less clear whether long-range signaling via pheromones plays a role in *C. elegans* aggregation (de Bono, Tobin, Davis, Avery, & Bargmann, 2002; Macosko et al., 2009). We removed pheromones from both *npr-1* and N2 animals using a *daf-22* mutation and found that the resultant pheromone-deficient strains aggregate to quantitatively similar levels compared with their pheromone-intact counterparts (Supplementry Figure S2A), thus supporting our focus on searching for interaction rules that are local.

One can conceive of some potential short-range mechanisms to promote aggregation. We considered posture changes and adhesion, but found no evidence for these to be major drivers of aggregation. Posture changes during worm locomotion may be informative of behavioral dynamics (Brown, Yemini, Grundy, Jucikas, & Schafer, 2013; Stephens, Johnson-Kerner, Bialek, & Ryu, 2008), so we investigated whether they inform behavioral changes during aggregation. To test this, we performed principal component analysis for the postures of lone versus in-cluster *npr-1* worms, and found them to be similar between the two categories (Supplementary Figure S2B). Thus, postural changes do not appear to be the cause of aggregation. Another known mechanism for aggregation in active matter systems is attraction between the moving objects (Redner, Baskaran, et al., 2013), but it is not known whether this applies to worms. Short-range attraction between worms may exist in the form of adhesion mediated through a liquid film (Gart et al. 2011), but we have no reason to believe this would differ between *npr-1* and N2 strains.

Reversal rates and speed depend on neighbor density more strongly in *npr-1* than in N2

Having excluded a few possible behavioral components from our consideration, we found experimental evidence that neighbor density-dependence of both reversal rates and motility speed differ between the two strains we studied.

Reversals have been previously observed as a behavior that may enable *npr*-1 to stay in aggregates (Rogers et al., 2006), but this had yet to be systematically quantified. Using our tracking of pharynx-labeled worms, we can quantify reversals inside aggregates, but at the cost of losing the exact outline of a cluster (since we only see the heads). Hence, we opted to avoid cluster definitions based on thresholding the distance between worms, and quantify individual worm behavior as a function of local density (Figure 3A) instead. Calculating the reversal rates relative to that of worms at low densities, we found that *npr-1* mutants reverse more at increased neighbor densities, while N2 do not (Figure 3B).

Next we calculated the speed distributions of individual worms, binned by local neighbor density. We found that both strains slow down when surrounded by many other worms, but the shift is much more pronounced for *npr-1* animals. *npr-1* worms move faster than N2 at low densities, showing a distinct peak at high speeds. As neighbor density increases, this high speed peak gradually becomes replaced by a peak at low speeds, so that the overall speed distribution for *npr-1* resembles that of N2 at very high densities. Thus, *npr-1* mutants and N2 show different density-

dependent changes in their respective speed profiles (Figure 3C).

Since the observed transition of the speed profiles could occur due to active behavioral changes as well as restricted movement in clusters, we also considered tracks of individual worms. Using body wall muscle-marked worms allowed us to obtain longer trajectories that could be joined for the duration of an entire movie, including cluster entry and exit events. We compared the speed of these tracks with visual assessment of when a worm entered or exited a cluster based on the proximity to pharynx-labeled worms. We show that worms are able to move inside of clusters and observed that speed changes can occur prior to cluster entry and exit events (Figure 3D, Supplementary Movie S2 and S3). This change of speed is neither purely mechanical nor a deterministic response to a certain neighbor density, and suggests a mechanism in which worms probabilistically switch between different speeds.

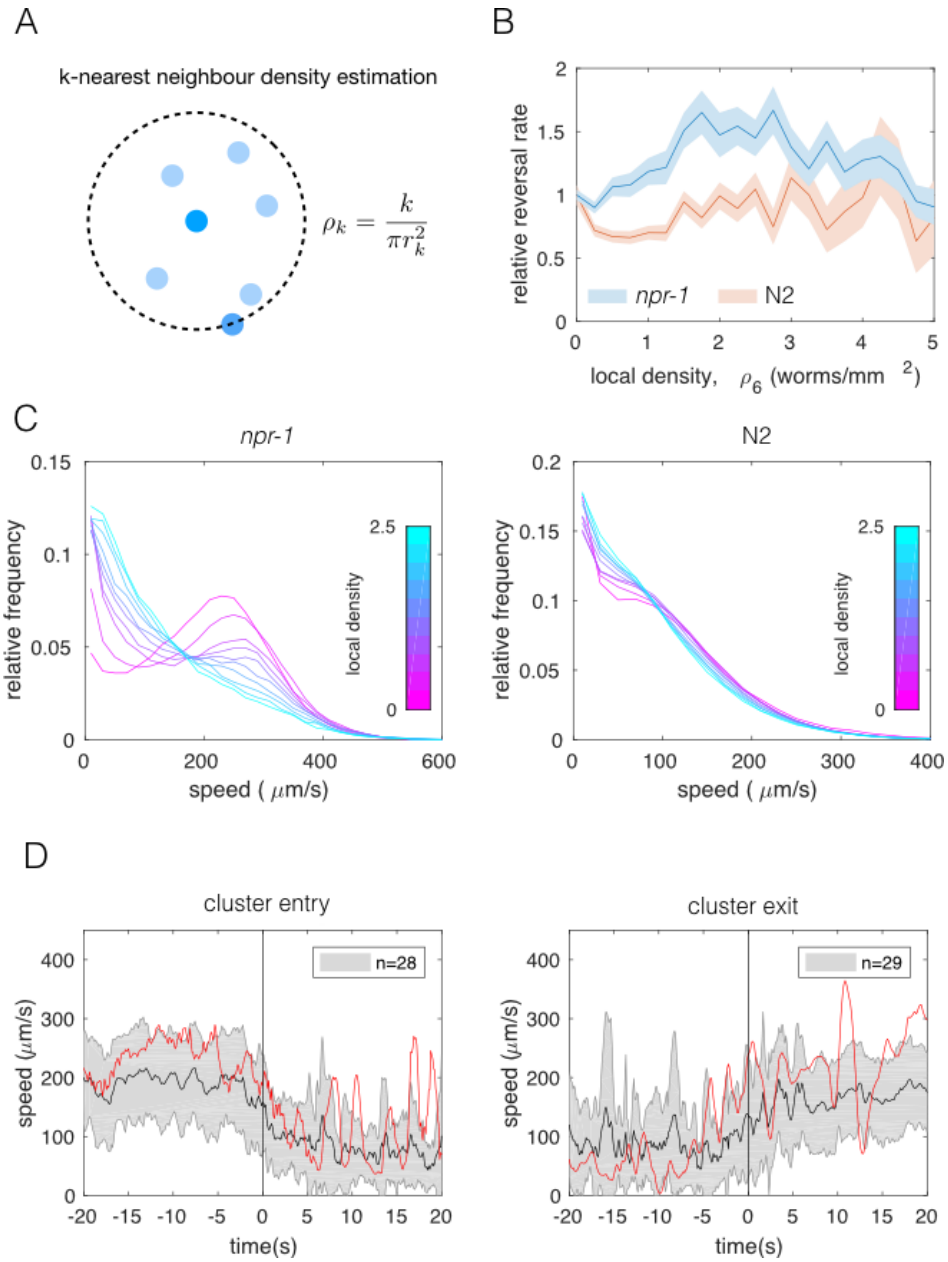

Figure 3. **Individual-level behavioral quantification**. A) Schematic explaining *k*-nearest neighbor density estimation. B) Relative rate of reversals as a function of local density (*k*-nearest neighbor density estimation with *k*=6) for *npr-1* (blue) and N2 (orange) strains. Lines show means and shaded area shows standard deviation (bootstrap estimate, 100 samples with replacement). C) Distributions of crawling speeds at different local neighbor densities for both strains. Lines show histograms of speeds for each density bin, and the color of the line indicated the density (blue is high, magenta is low). D) Midbody absolute speed for manually annotated cluster entry events (left, n=28) and exit events (right, n=29). Each event was manually identified, with time 0 representing the point where the head or tail of a worm starts to enter (left) or exit (right) an existing cluster. Skeleton *xy*-coordinates were linearly interpolated for missing frames for each event, before being used to calculate midbody speed extending 20 seconds on both sides of time 0 of the event. Speeds were smoothed over a one-second window. Shading represents standard deviation across events. Red lines show the midbody absolute speed of one representative event, as shown in Supplementary Movie S2 (left) or Supplementary Movie S3 (right).

Spatial statistics show group-level differences between *npr-1* and N2 animals

The differences in aggregation behavior between *npr*-1 and N2 are visually striking, but previous quantification has been limited to the number of animals in clusters. Using the tracked positions of pharynx-labeled worms (Figure 4A), we calculated the pair-correlation function (Figure 4B), commonly used to quantify aggregation in cellular and physical systems (Gurry, Kahramanogullari, & Endres, 2009). We also computed a hierarchical clustering (linkage function in Matlab) of worm positions (Figure 4C), which is calculated from the same pairwise distances but emphasizes larger scale structure. Using both measures, we found that as a population, *npr-1* animals show quantifiably higher levels of aggregation than N2, especially at scales up to 1 mm (pair-correlation "S_1", Figure 4D) and 2 mm (hierarchical clustering "S_2", Figure 4E). We also quantified aggregation using scalar spatial statistics, namely the average standard deviation ("S_3") and kurtosis ("S_4") of the distribution of positions. This confirmed that the positions of *npr-1* worms are less spread-out and more heavy-tailed than those of N2 (Figure 4D).

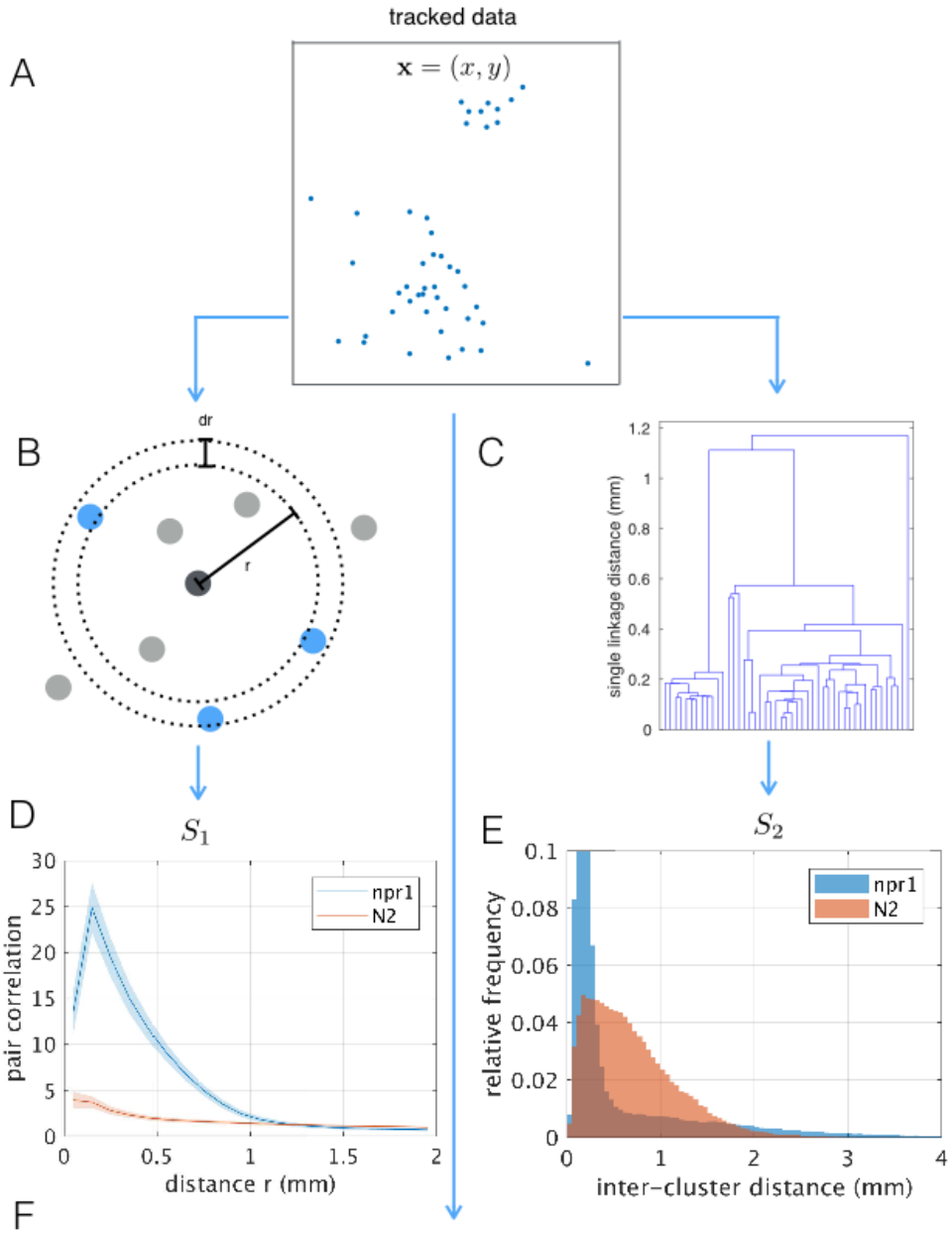

	npr-1	N2
$S_3 = \langle \sigma(\mathbf{x}) \rangle_t$	1.9±0.1	2.4±0.1
$S_4 = \langle \mathrm{Kurt}(\mathbf{x}) \rangle_t$	5.4±0.6	2.5±0.1

Figure 4. Population-level behavioral quantification. A) Positions of *npr-1* worms in example frame. B) Schematic explaining positional correlation function (S_1, *pcf*). The *pcf* counts the number of neighbors at a distance *r*, normalized by the expectation for a uniform distribution. C) Example dendrogram from which hierarchical clustering branch length distributions (S_2) can be calculated. D) Positional correlation function for *npr-1* (blue) and N2 (orange). Lines show mean and shaded area shows standard error of the mean. E) Hierarchical clustering branch length distributions for *npr-1* (blue) and N2 (orange). Histograms show relative frequency of inter-cluster distances (single linkage distance in agglomerative hierarchical clustering, equivalent to the branch lengths in the example dendrogram in (C)). F) Mean standard deviation (S_3) and kurtosis (S_4) of the positions of worms, with the mean taken over frames sampled.

Agent-based model captures different aggregation phenotypes

To test whether the individual behavioral differences measured between *npr*-1 and N2 worms are sufficient to give rise to the observed differences in aggregation, we constructed a phenomenological model of worm movement and interactions. The model is made up of self-propelled agents (Figure 5A), and includes density-dependent interactions motivated by the experimental data, namely reversals at the edge of a cluster (Figure 5B) and a switch between movement at different speeds (Figure 5C). We ignored spontaneous reversals outside of clusters as these were only rarely observed in our experiments. See Supplementary Methods for further discussion of the model construction. As a model of collective behavior this differs from those commonly considered in the literature, such as the Vicsek model (Vicsek, Czirók, Ben-Jacob, Cohen, & Shochet, 1995) and its many related variants. Such models typically feature attractive forces or align the direction of motion at ranges much longer than the size of the moving objects, and result in flocking or clustering with global alignment (Figure 5D), which we do not observe in our experimental data. In contrast, our model needs to produce dynamic, disordered aggregates (Figure 1B, Figure 2A and Supplementary Movie S1), and should primarily rely on short-range interactions that are motivated by behaviors measured in our data.

We initially ran a coarse parameter sweep, sampling uniformly in the two-dimensional parameter space associated with the density-dependence of reversals and speed switching. This demonstrates that our model can capture different aggregation phenotypes from solitary movement to aggregation (Figure 5E), by varying just two free parameters. Inspection of the model simulations shows that each behavior alone (just reversals or slowing) does not give the same level of aggregation as when both parameters are modulated (Figure 5E), so that using both behavioral components proves important. Quantifying the aggregation and comparing it to the *npr-1* experiment, however, highlights incomplete quantitative agreement with both the pair correlation function and hierarchical clustering distribution (Figure 5F). Thus, we reasoned additional interactions may be required to match the experimentally observed behaviors.

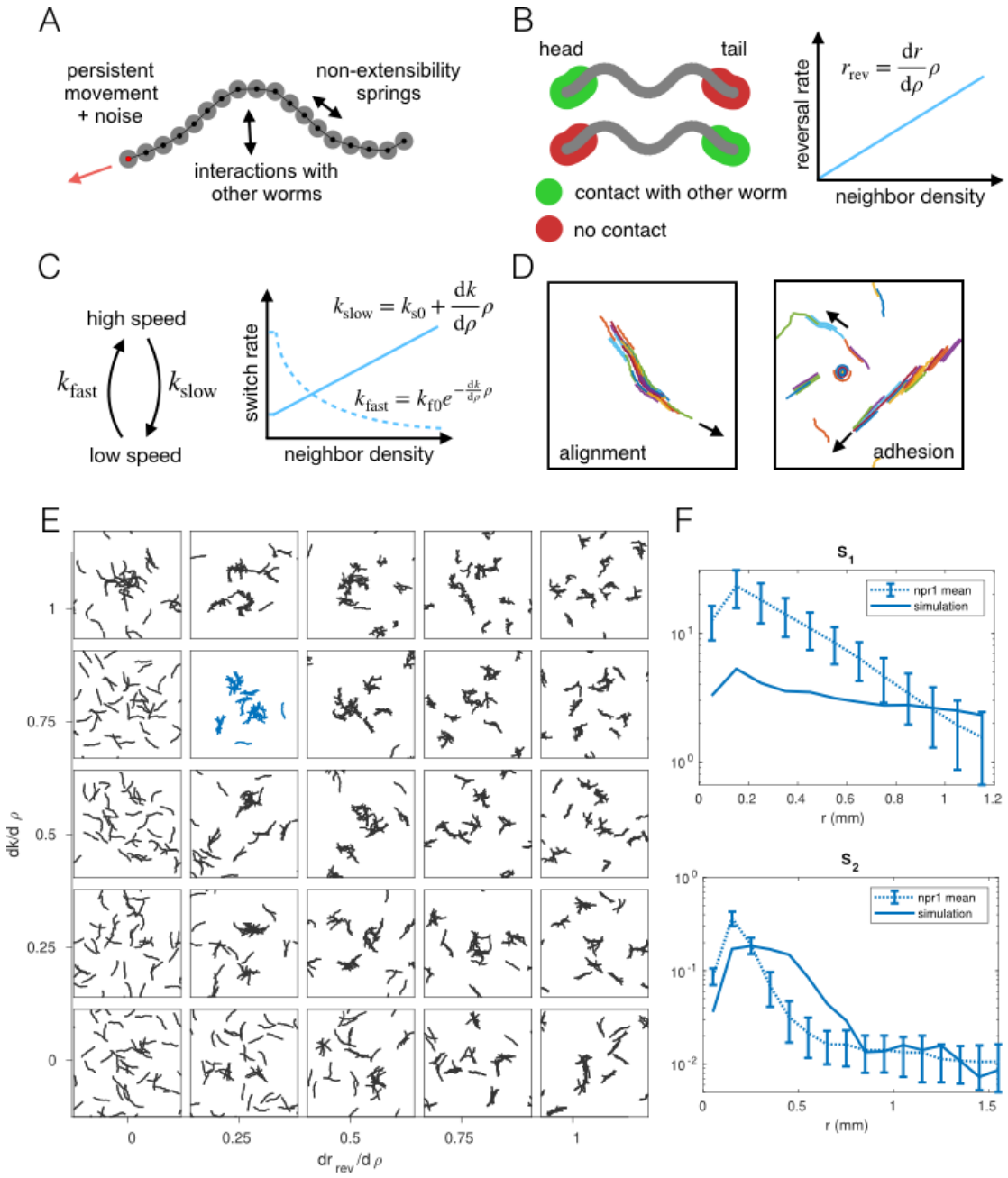

Figure 5. Agent-based modeling of emergent behavior. A) Schematic of individual worm in the agent-based model. Each worm made up of *M* nodes (here *M*=18), connected by springs to enforce non-extensibility. Each node undergoes self-propelled movement, with the head node (red dot) undergoing a persistent random walk, and the rest of the nodes follow in the direction of the body. B) Schematic of simulated reversals upon exiting a cluster. Each worm registers contact at the first and last 10% of its nodes within a short interaction radius. If contact is registered at one of the head/tail, but not the other, the worm is leaving a cluster and thus reverses with a Poisson rate dependent on the local density. C) Schematic of density-dependent switching between movement speeds. Worms stochastically switch between slow and fast movement with Poisson rates k_{slow} and k_{fast}, which increase linearly and decrease exponentially with neighbor density, respectively. D) Snapshots of simulations with commonly considered aggregation mechanisms, which produce unrealistic behavior for worm simulations, with flocking and highly aligned clustering. Arrows indicate the direction of movement of large clusters. E)

Phase portrait of model simulations, showing snapshots from the last 10% of each simulation, for different values of the two free parameters: density-dependence of the reversal rate and density-dependence of speed-switching (here k_{slow} = k_{fast}). F) Summary statistics S_1 (pair correlation, top) and S_2 (hierarchical clustering, bottom) for the simulation which most closely matches the experimental data for the *npr-1* strain (blue panel in (E)).

Adding a medium-range taxis interaction promotes stronger aggregation

To explore improvements in clustering, we extended the model to four parameters: density-dependent increase in reversal frequency, density-dependent increase in slowing, density-dependent decrease in speeding up, and medium-range taxis interaction between worms. The taxis interaction biases the movement of a worm towards groups of its neighbors, has a range equal to the length of a worm (the natural intermediate length scale in our system), and is weighted inversely proportionally to the distance of neighbors (see Supplementary Methods for details).

We selected the closest matching simulations from about 2000 simulations for *npr*-1 and about 400 simulations for N2, sampled from a reduced prior parameter space (see Supplementary Methods), equally weighting all four summary statistics. Results from our extended model (Supplementary Movie S4 and S5) show markedly improved quantitative agreement with the experiments (Figure 6), though further simulations would be needed to determine the posterior distributions of parameters.

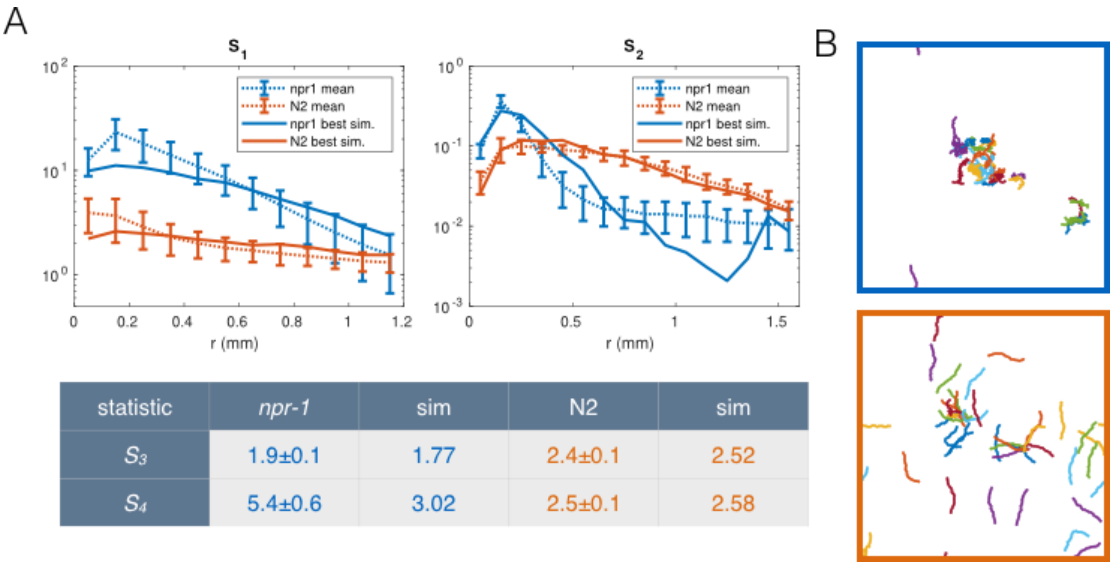

statistic	*npr-1*	sim	N2	sim
S_3	1.9±0.1	1.77	2.4±0.1	2.52
S_4	5.4±0.6	3.02	2.5±0.1	2.58

Figure 6. Extended model better captures quantitative aggregation phenotypes. A) Summary statistics: S_1: pair correlation function; S_2: hierarchical clustering distribution; S_3: standard deviation of positions; S_4: kurtosis of positions. Solid lines show the closest matching simulations, dashed lines show experimental means, and error bars show standard deviation of 13 (*npr-1*) and 9 (N2) replicates. B) Sample snapshot of the closest matching simulations for *npr-1* (top) and N2 (bottom).

Extending the model with food-depletion captures dynamic swarming

We made one final extension in our model to allow the local depletion of food. Food is initially distributed uniformly, and becomes depleted locally by worm feeding (see Supplementary Methods for details). Absence of food suppresses the switch to slow speeds, thus causing worms to speed up when food is locally depleted.

Selecting the parameter combination best matching the *npr*-1 strain (Figure 6) and an appropriate food depletion rate, the resulting simulation produced long-time dynamics qualitatively representative of the experimentally observed swarming (Figure 7, Supplementary Movie S6). Thus, the model indicates that dynamic swarming of *npr-1* aggregates may be explained as an emergent phenomenon resulting from individual locomotion, and that the same behavioral mechanisms that produce steady-state aggregates, when coupled with local food depletion, produce the observed swarming behavior.

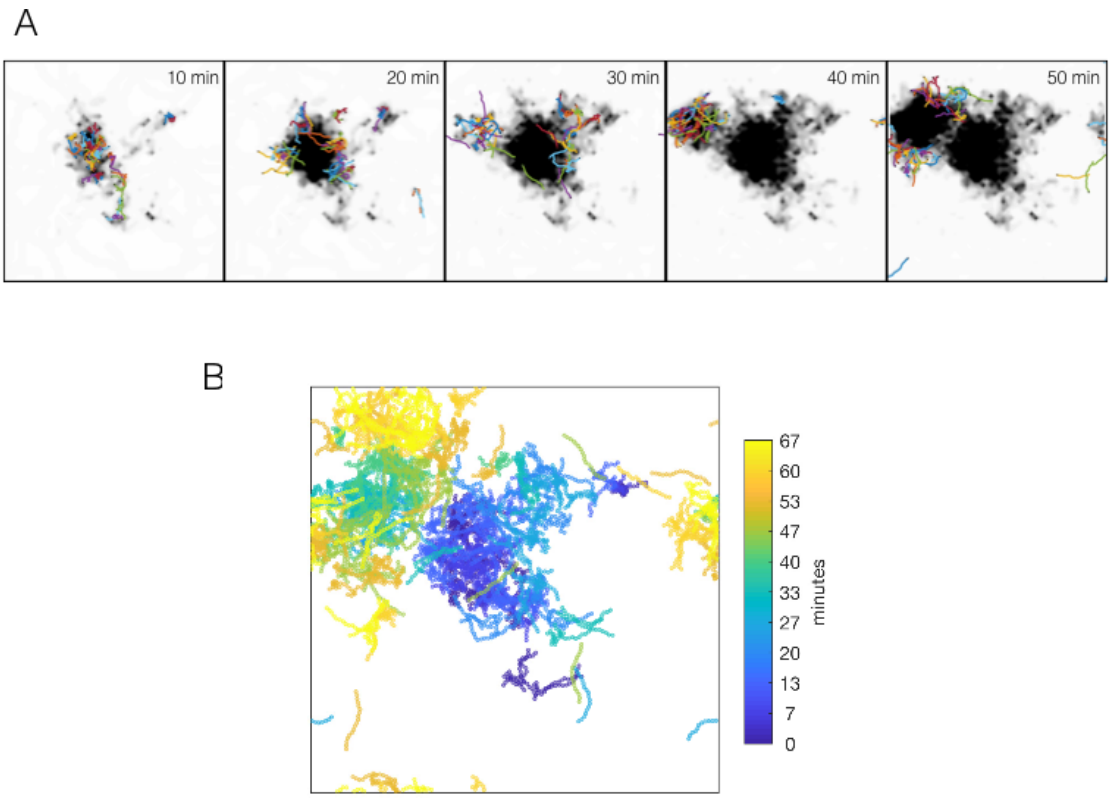

Figure 7. Simulations capture dynamic swarming. A) Snapshots of aggregating simulation with food depletion. Background color shows food concentration (arbitrary units) with white indicating high food and black indicating no food. B) Visualization of worm positions in (A) over time, showing cluster displacement of cluster. Note the periodic boundary conditions.

Discussion

We have investigated the mechanisms of aggregation and swarming in *C. elegans* collective feeding using a combination of quantitative imaging and computational modeling. First, we quantified individual- and population-level behaviors in two strains with drastically different feeding phenotypes: social *npr-1* mutants and more solitary worms from the common laboratory strain N2. We then built an agent-based computational model to implement the identified individual-level behavioral differences, and test whether these are sufficient to explain differences in group-level aggregation phenotype between the two strains. Reversals and slowing have been previously proposed as behavioral components important for aggregation (Rogers et al., 2006). Here, for the first time we explicitly tested their sufficiency to produce aggregation, in addition to providing quantitative details of these behaviors in aggregating worms. Our modeling results show that a combination of increased reversals upon leaving aggregates and a neighbor density-dependent increase in speed switching rates captures various aggregation phenotypes, but there was a noticeable mismatch in quantitative clustering details between simulations and experiments until a medium-range taxis interaction was added. This taxis may be attributed to a shallow O_2 or CO_2 gradient created by a worm cluster (which we discuss below), to additional diffusible molecules unaffected by *daf-22*, or to yet another unknown mechanism. Lastly, we extend the model to include food depletion, and thus reproduce the dynamic swarming behavior seen in *npr-1* worms over time. This suggests that the same behavioral mechanisms indeed underlie both steady-state aggregation and dynamic swarming at different time scales during *C. elegans* collective feeding.

We focused on identifying behavioral components giving rise to aggregation, while remaining agnostic as to the sensory cues causing the behaviors, i.e., whether the density-dependent interactions and taxis are mediated by oxygen concentration, CO_2, or another signal. The density-dependent interactions could arise from local molecular signaling, or be mediated through contact-sensing, and the $1/r$ dependence of the taxis interaction is compatible with a diffusible, non-degrading factor (such as CO_2, or O_2 depletion; dependence would be exponential for a degrading molecule, such as pheromones). Previous work suggests oxygen avoidance as a major explanation of behavior changes upon entering or leaving aggregates (Rogers et al., 2006). That hypothesis states that oxygen consumption by worms locally lowers O_2 concentration, thus creating conditions preferred by *npr-1* mutants and promoting their aggregation. To support this, Rogers et al. (2006) report measurement of steep O_2 gradients inside worm clusters. We think such steep gradient can be ruled unlikely by reaction-diffusion calculations: the diffusion of oxygen through worm tissue, or their oxygen consumption, would need to be several orders of magnitude different to create O_2 gradients as steep as reported by Rogers et al. (Supplementary Figure S3). However, as worms have been reported to respond even to small changes in oxygen concentration (McGrath et al., 2009), the behavior sufficient for aggregation may still be mediated through the feasible, shallower local oxygen gradients. Therefore, our agent-based simulations are entirely compatible with this picture. Further work quantifying the behavior of individual worms at different oxygen concentrations may help to distinguish oxygen as a direct cue or part of the “sensory triggers that can initiate social behavior by activating chemotaxis or mechanotaxis” (Gray et al., 2004); in other words, whether it is just necessary or also sufficient to explain aggregation.

The purpose of our modeling approach was to capture the emergent behavior, which should be independent of many microscopic details. In the interest of simplicity and computational efficiency, we thus favored a more abstract representation than

existing models of single-worm motility (Boyle et al. 2012; Cohen & Ranner 2017; Majmudar et al. 2012; Keaveny & Brown 2017). We furthermore excluded long-range interactions such as chemotaxis and pheromone signaling, and did not consider memory effects, e.g. of oxygen exposure (Fenk & de Bono, 2017), or time-dependent parameters. Our results indicate these are not crucial for aggregation, though it remains feasible that they could be necessary to capture transient behavior during initial aggregation. Additional interactions are straight-forward to implement in our model, but as our model is relatively intensive computationally (over an hour for longer simulations), sampling higher dimensional parameter spaces would provide a challenge.

In the broader context of collective behavior, *C. elegans* bridges the gap between the commonly studied micro- and macro-scales, and finding the behavioral rules underlying this mesoscale system indeed allow us to examine overarching principles governing collective behavior across scales. Both key behavioral rules identified here for *C. elegans* aggregation also find importance in collective systems at other scales. Spontaneous reversals have been implicated in bacterial aggregation at the microscale (Starruss et al., 2012; Thutupalli, Sun, Bunyak, Palaniappan, & Shaevitz, 2015). By contrast, aggregating worms reverse mainly in response to leaving a cluster, thus requiring more complex sensory processing and behavioral response than seen in bacterial systems. Changes in movement speed, too, have been considered more widely in many microscale theoretical systems in the field of motility-induced phase transitions (Redner, Hagan, et al. 2013; Großmann et al. 2016). The emergent phenomena observed in models of interacting particles generally range from diffusion-limited aggregation to jamming at high volume fractions to flocking of self-propelled rods through volume exclusion (in two-dimensions). Aggregation in *C. elegans* occurs at much lower numbers of objects (tens of worms) and lower densities (area fraction of 4-6%) than typically studied in this field (thousands of objects at area fractions of 20-80%), and the density dependence of motility changes again emphasizes the role of more complex sensing and behavioral modulations. Thus, the mesoscale collective behavior of *C. elegans* indeed draws from both ends of the size and complexity spectrum, linking the physical mechanisms familiar from microscopic cellular and active matter systems with the behavioral repertoire of larger multicellular organisms.

A key advantage of using *C. elegans* to study collective behavior is the opportunity to experimentally control and perturb the system, which is rarely possible with other organisms. One may envisage using reversal, dwelling, and oxygen-sensing mutants to experimentally modify our key behavioral parameters, or employing optogenetic methods to apply acute changes to the system. Thus, there are ample opportunities for future studies to further integrate the experimental and theoretical methods in the study of *C. elegans* collective behavior. The insights generated in this paper also offer scope for explaining variations in collective behavior of wild isolates. Our work presented here focused on explaining the differences in aggregation between the N2 and *npr*-1 mutant strains. Many wild isolate strains show different degrees of aggregation (de Bono & Bargmann 1998), but the quantitative details remain scant. The approach presented here offers the possibility to explain the variability of collective behaviors seen in the wild isolates based on the modulation of a few behavioral components, and suggests a combined experimental-computational pipeline for such an endeavor.

Materials and Methods

Strain maintenance and bleach synchronization

C. elegans strains used in this study are listed in Supplementary Table 1. All animals were grown on *E. coli* OP50 at 20°C as mixed-stage cultures and maintained as described (Brenner, 1974). All animals used in imaging experiments are synchronized young adults obtained by bleaching gravid hermaphrodites grown on *E. coli* OP50 under uncrowded and unstarved conditions, allowing isolated eggs to hatch and enter L1 diapause on unseeded plates overnight, and re-feeding starved L1's for 65-72 hours on OP50.

Bright field high-number swarming imaging

The strain used here (Figure 1A) is DA609. On imaging day, synchronized adults were collected and washed in M9 buffer twice before several hundred animals were transferred to a seeded 90 mm NGM plate using a glass pipette. After M9 is absorbed into the media, ten-hour time-lapse recordings were taken with a Dino-Lite camera (AM-7013MT) at room temperature (20°C) using the DinoCapture 2.0 software (v1.5.3.c) for the maximal field of view. Two independent replicates were performed.

Bright field standard swarming imaging

The strains used here (Figure 1B) are OMG2 and OMG10. Prior to collecting the full dataset, a single batch OP50 was grown overnight, diluted to OD_{600} = 0.75, aliquoted for use on each imaging day, and stored at 4°C until use. Imaging plates were 35 mm Petri dishes containing 3.5 mL low peptone (0.013% Difco Bacto) NGM agar (2% Bio/Agar, BioGene) to limit bacteria growth. A separate batch of plates was poured exactly seven days before each imaging day, stored at 4°C, and dried at 37°C overnight with the agar side down before imaging. The center of an imaging plate was seeded with a single 20 µL spot of cold diluted OP50 one to three hours before imaging. The overnight plate drying step allowed the bacteria to quickly dry atop the media in order to achieve a more uniform lawn, by minimizing the "coffee ring" effect that would thicken the circular edge of the bacteria lawn. For each imaging day, synchronized young adults were collected and washed in M9 buffer twice before 40 animals were transferred to a seeded imaging plate using a glass pipette.

Imaging commenced immediately following animal transfer in a liquid drop, on a custom-built six-camera rig equipped with Dalsa Genie cameras (G2-GM10-T2041). Seven-hour recordings with red illumination (630 nm LED illumination, CCS Inc.) were taken at 25 Hz using Gecko software (v2.0.3.1), whilst the rig maintained the imaging plates at 20°C throughout the recording durations. Images were segmented in real time by the Gecko software. The recordings were manually truncated post-acquisition to retain aggregation and swarming dynamics only. The start time was defined as the moment when the liquid dried and the all the worms crawled out from the initial location of the drop, and the end time was when the food was depleted and worms dispersed with increased crawling speed. Twelve independent replicates were performed for each strain.

Bright field big patch swarming imaging

The experiments here (Supplementary Figure S1A) are identical to those in the bright field standard swarming imaging, except for two differences. First, the imaging plates were seeded with a 50 µL spot of diluted OP50 (OD_{600} = 0.38) and allowed to

inoculate overnight at room temperature before being used for imaging the next day. Second, recordings were taken over 20 hours instead of seven. Eight independent replicates were performed for each strain.

Bright field pheromone imaging

The strains used here (Supplementary Figure 2A) are OMG2, OMG10, DR476, and AX994. Bacteria aliquots and imaging plates were prepared as in the bright field standard swarming imaging assay. For each imaging day, synchronized young adults were collected and washed in M9 buffer twice before 40 animals were transferred to a seeded imaging plate using a glass pipette. After M9 was absorbed into the media following worm transfer in liquid, imaging plates containing the animals were subjected to a gentle vibration at 600 rpm for 10 s on a Vortex Genie 2 shaker (Scientific Industries) to disburse animals and synchronize aggregation start across replicates. Imaging commenced 20 s after the vibration finish, using the same rig set-up as swarming imaging above, except one-hour recordings were taken. Images were segmented in real time by the Gecko software. At least eight independent replicates were performed for each strain. Automated animal tracking was performed post-acquisition using Tierpsy Tracker software (http://ver228.github.io/tierpsy-tracker/, v1.3), which we developed in-house (Javer et al., 2018). Images with were tracked with customized parameters to create centroid trajectories, 49-point worm skeletons, and a battery of features.

Fluorescent aggregation imaging

The strains used here (Figure 2) are OMG2, OMG10, OMG19, and OMG24. One-color imaging consisted of pharynx-GFP labeled worms only, whereas two-color imaging also included a small number of body wall muscle-RFP labeled worms that were recorded simultaneously on a separate channel (thus readily segmented from the rest of the worms). The latter was necessary to follow individuals over a long period of time, particularly while inside a cluster, as frequent pharynx collisions inside clusters lead to lost individual identities and broken trajectories. For two-color imaging, animals with different fluorescent markers were mixed in desired proportion (1-3 red animals out of 40 per experiment) during the washing stage before being transferred together for imaging.

The data collection paradigm was identical to the bright field pheromone imaging assay in terms of bacteria aliquot and imaging plate preparation and vibration implementation following animal transfer. The only difference is that image acquisition was performed on a DMI6000 inverted microscope (Leica) equipped with a 1.25x PL Fluotar objective (Leica), a TwinCam LS image splitter (Cairn) with a dichroic cube (Cairn), and two Zyla 5.5 cameras (Andor) to enable simultaneous green-red imaging with maximal field of view. One-hour recordings were taken with constant blue (470 nm, 0.8A) and green (cool white, 1.4A) OptoLED illumination (Cairn), and images were acquired with 100 ms exposure at 9 Hz using Andor Solis software (v4.29.30005.0). The microscopy room was maintained at 21°C throughout the recording durations. Ten or more independent replicates were performed for each strain. We were able to reproduce stereotyped aggregation dynamics across replicates under our experimental paradigm (Supplementary Figure S1B). Image segmentation and automated animal tracking was performed post-acquisition using Tierpsy Tracker software (v1.3) with customized parameters, to create centroid trajectories, obtain two-point skeleton from pharynx-labeled individuals and 49-point midline skeletons from body wall muscle-marked ones, and extract various features. For body wall muscle-marked animals, trajectories were manually joined where broken due to tracking errors.

Fluorescent aggregation tracking data analysis

Tracked blobs were filtered for minimum fluorescence intensity and maximum area, to exclude any larvae and tracking artifacts, respectively, which appeared on the occasional plate. Local worm densities around each individual were calculated using *k*-nearest neighbor density estimation, where the density is *k* divided by the area of a circle encompassing the *k*-th nearest neighbor. We chose $k = 6 \approx \sqrt{N}$ and verified based on visual assessment that the overall distribution of local densities changes very little with increasing *k*.

Reversals were detected based on a change of sign of speed from positive to negative, which was calculated from the dot-product of the skeleton vector (of the pharynx) and the velocity vector, and smoothed with a moving average over half a second. We only counted reversals that were at least 50 μm in length, and that moved at least half a pixel per frame before and after the reversal. Reversal events thus detected where binned by their local density. For each density bin, reversal rate was estimated as the number of events divided by the time spent in forward motion for that bin. The variability was estimated using a subsampling bootstrap: the reversal rate was estimated 100 times, sampling worm-frames with replacement, and estimating mean and standard deviation.

Summary statistics of aggregation, such as pair-correlation and hierarchical clustering, where calculated as described in the supplementary computational methods.

Acknowledgements

We thank Camille Straboni for the imaging data shown in Figure 1A, Ivan Croydon Veleslavov for to the code for parameter inference, and Suhail Islam for computational support. This work is supported by a BBSRC/UK Research and Innovation research grant (BB/N00065X/1).

Competing interests

The authors declare no competing interests.

References

Bialek, W., Cavagna, A., Giardina, I., Mora, T., Silvestri, E., Viale, M., & Walczak, A. M. (2012). Statistical mechanics for natural flocks of birds. *Proceedings of the National Academy of Sciences*, *109*(13), 4786–4791. https://doi.org/10.1073/pnas.1118633109

Boyle, J. H., Berri, S., & Cohen, N. (2012). Gait Modulation in C. elegans: An Integrated Neuromechanical Model. *Frontiers in Computational Neuroscience*, *6*. https://doi.org/10.3389/fncom.2012.00010

Brenner, S. (1974). The genetics of Caenorhabditis elegans. *Genetics*, *77*(1), 71–94.

Brown, A. E. X., Yemini, E. I., Grundy, L. J., Jucikas, T., & Schafer, W. R. (2013). A dictionary of behavioral motifs reveals clusters of genes affecting Caenorhabditis elegans locomotion. *Proceedings of the National Academy of Sciences*, *110*(2), 791–796. https://doi.org/10.1073/pnas.1211447110

Busch, K. E., Laurent, P., Soltesz, Z., Murphy, R. J., Faivre, O., Hedwig, B., … de Bono, M. (2012). Tonic signaling from O2 sensors sets neural circuit activity and behavioral state. *Nature Neuroscience*, *15*(4), 581–591. https://doi.org/10.1038/nn.3061

Cheung, B. H. H., Cohen, M., Rogers, C., Albayram, O., & de Bono, M. (2005). Experience-Dependent Modulation of C. elegans Behavior by Ambient Oxygen. *Current Biology*, *15*(10), 905–917. https://doi.org/10.1016/j.cub.2005.04.017

Cohen, N., & Ranner, T. (2017). A new computational method for a model of C. elegans biomechanics: Insights into elasticity and locomotion performance. *arXiv*, 1702.04988.

de Bono, M., & Bargmann, C. I. (1998). Natural variation in a neuropeptide Y receptor homolog modifies social behavior and food response in C. elegans. *Cell*, *94*(5), 679–689.

de Bono, M., Tobin, D. M., Davis, M. W., Avery, L., & Bargmann, C. I. (2002). Social feeding in Caenorhabditis elegans is induced by neurons that detect aversive stimuli. *Nature*, *419*(6910), 899–903. https://doi.org/10.1038/nature01169

Fenk, L. A., & de Bono, M. (2017). Memory of recent oxygen experience switches pheromone valence in Caenorhabditis elegans. *Proceedings of the National Academy of Sciences of the United States of America*, *114*(16), 4195–4200. https://doi.org/10.1073/pnas.1618934114

Gart, S., Vella, D., & Jung, S. (2011). The collective motion of nematodes in a thin liquid layer. *Soft Matter*, *7*(6), 2444. https://doi.org/10.1039/c0sm01236j

Gray, J. M., Karow, D. S., Lu, H., Chang, A. J., Chang, J. S., Ellis, R. E., … Bargmann, C. I. (2004). Oxygen sensation and social feeding mediated by a C. elegans guanylate cyclase homologue. *Nature*, *430*(6997), 317–322. https://doi.org/10.1038/nature02714

Großmann, R., Peruani, F., & Bär, M. (2016). Mesoscale pattern formation of self-propelled rods with velocity reversal. *Physical Review E*, *94*(5), 1–7. https://doi.org/10.1103/PhysRevE.94.050602

Gurry, T., Kahramanogullari, O., & Endres, R. G. (2009). Biophysical Mechanism for Ras-Nanocluster Formation and Signaling in Plasma Membrane. *PLoS ONE*, *4*(7), e6148. https://doi.org/10.1371/journal.pone.0006148

Jang, H., Levy, S., Flavell, S. W., Mende, F., Latham, R., Zimmer, M., & Bargmann, C. I. (2017). Dissection of neuronal gap junction circuits that regulate social behavior in *Caenorhabditis elegans*. *Proceedings of the National Academy of Sciences*, *1*(28), 201621274. https://doi.org/10.1073/pnas.1621274114

Javer, A., Currie, M., Lee, C. W., Hokanson, J., Li, K., Martineau, C. N., … Brown, A. E. (2018). An open source platform for analyzing and sharing worm behavior data. *bioRxiv*, 377960. https://doi.org/10.1101/377960

Katz, Y., Tunstrøm, K., Ioannou, C. C., Huepe, C., & Couzin, I. D. (2011). Inferring the structure and dynamics of interactions in schooling fish. *Proceedings of the National Academy of Sciences*, *108*(46), 18720–18725. https://doi.org/10.1073/pnas.1107583108

Keaveny, E. E., & Brown, A. E. X. (2017). Predicting path from undulations for C. elegans using linear and nonlinear resistive force theory. *Physical Biology*, *14*(2), 025001. https://doi.org/10.1088/1478-3975/aa5ce6

Köhler, S., Schaller, V., & Bausch, A. R. (2011). Collective Dynamics of Active Cytoskeletal Networks. *PLOS ONE*, *6*(8), e23798. https://doi.org/10.1371/journal.pone.0023798

Macosko, E. Z., Pokala, N., Feinberg, E. H., Chalasani, S. H., Butcher, R. A., Clardy, J., & Bargmann, C. I. (2009). A hub-and-spoke circuit drives pheromone attraction and social behaviour in C. elegans. *Nature*, *458*(7242), 1171–1175. https://doi.org/10.1038/nature07886

Majmudar, T., Keaveny, E. E., Zhang, J., & Shelley, M. J. (2012). Experiments and theory of undulatory locomotion in a simple structured medium. *Journal of The Royal Society Interface*. https://doi.org/10.1098/rsif.2011.0856

McGrath, P. T., Rockman, M. V., Zimmer, M., Jang, H., Macosko, E. Z., Kruglyak, L., & Bargmann, C. I. (2009). Quantitative Mapping of a Digenic Behavioral Trait Implicates Globin Variation in C. elegans Sensory Behaviors. *Neuron*, *61*(5), 692–699. https://doi.org/10.1016/j.neuron.2009.02.012

Palo, G. D., Yi, D., & Endres, R. G. (2017). A critical-like collective state leads to long-range cell communication in Dictyostelium discoideum aggregation. *PLOS Biology*, *15*(4), e1002602. https://doi.org/10.1371/journal.pbio.1002602

Pearce, D. J. G., Miller, A. M., Rowlands, G., & Turner, M. S. (2014). Role of projection in the control of bird flocks. *Proceedings of the National Academy of Sciences*, *111*(29), 10422–10426. https://doi.org/10.1073/pnas.1402202111

Peruani, F., Starruß, J., Jakovljevic, V., Søgaard-Andersen, L., Deutsch, A., & Bär, M. (2012). Collective Motion and Nonequilibrium Cluster Formation in Colonies of Gliding Bacteria. *Physical Review Letters*, *108*(9), 098102. https://doi.org/10.1103/PhysRevLett.108.098102

Redner, G. S., Baskaran, A., & Hagan, M. F. (2013). Reentrant phase behavior in active colloids with attraction. *Physical Review E*, *88*(1), 012305. https://doi.org/10.1103/PhysRevE.88.012305

Redner, G. S., Hagan, M. F., & Baskaran, A. (2013). Structure and dynamics of a phase-separating active colloidal fluid. *Physical Review Letters*, *110*(5), 1–5. https://doi.org/10.1103/PhysRevLett.110.055701

Reynolds, C. W. (1987). Flocks, herds and schools: A distributed behavioral model. *ACM SIGGRAPH Computer Graphics*, *21*(4), 25–34. https://doi.org/10.1145/37402.37406

Rogers, C., Persson, A., Cheung, B., & de Bono, M. (2006). Behavioral motifs and neural pathways coordinating O2 responses and aggregation in C. elegans. *Current Biology*, *16*(7), 649–659. https://doi.org/10.1016/j.cub.2006.03.023

Shoyama, T., Shimizu, Y., & Suda, H. (2009). Decline in oxygen consumption correlates with lifespan in long-lived and short-lived mutants of Caenorhabditis elegans. *Experimental Gerontology*, *44*(12), 784–791. https://doi.org/10.1016/j.exger.2009.09.006

Srinivasan, J., Kaplan, F., Ajredini, R., Zachariah, C., Alborn, H. T., Teal, P. E. A., … Schroeder, F. C. (2008). A blend of small molecules regulates both mating and development in Caenorhabditis elegans. *Nature*, *454*(7208), 1115–1118. https://doi.org/10.1038/nature07168

Starruss, J., Peruani, F., Jakovljevic, V., Sogaard-Andersen, L., Deutsch, A., & Bar, M. (2012). Pattern-formation mechanisms in motility mutants of Myxococcus xanthus. *Interface Focus*, *2*(6), 774–785. https://doi.org/10.1098/rsfs.2012.0034

Stephens, G. J., Johnson-Kerner, B., Bialek, W., & Ryu, W. S. (2008). Dimensionality and dynamics in the behavior of C. elegans. *PLoS Computational Biology*, *4*(4). https://doi.org/10.1371/journal.pcbi.1000028

Suda, H., Shouyama, T., Yasuda, K., & Ishii, N. (2005). Direct measurement of oxygen consumption rate on the nematode Caenorhabditis elegans by using an optical technique. *Biochemical and Biophysical Research Communications*, *330*(3), 839–843. https://doi.org/10.1016/j.bbrc.2005.03.050

Thutupalli, S., Sun, M., Bunyak, F., Palaniappan, K., & Shaevitz, J. W. (2015). Directional reversals enable Myxococcus xanthus cells to produce collective one-dimensional streams during fruiting-body formation. *Journal of The Royal Society Interface*, *12*(109), 20150049. https://doi.org/10.1098/rsif.2015.0049

Vicsek, T., Czirók, A., Ben-Jacob, E., Cohen, I., & Shochet, O. (1995). Novel Type of Phase Transition in a System of Self-Driven Particles. *Physical Review Letters*, *75*(6), 1226–1229. https://doi.org/10.1103/PhysRevLett.75.1226

White, J. G., Southgate, E., Thomson, J. N., & Brenner, S. (1986). The Structure of the Nervous System of the Nematode Caenorhabditis elegans. *Philosophical Transactions of the Royal Society B: Biological Sciences*, *314*(1165), 1–340. https://doi.org/10.1098/rstb.1986.0056

Supplementary Material

for

Common behavioral mechanisms underlie *C. elegans* aggregation and swarming

S. Serena Ding, Linus J. Schumacher, Avelino Javer, Robert G. Endres, André E. X. Brown

Supplementary Figures

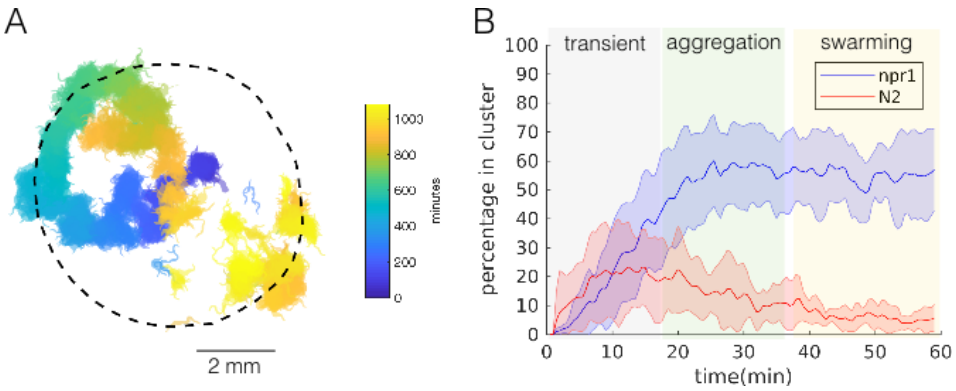

Supplementary Figure S1. *npr-1* aggregation and swarming dynamics. A) Forty *npr-1* animals swarm over a big food patch, following a persistent random walk. More than one large moving clusters co-exist towards the end of the movie (orange and yellow), and a cluster (orange) disperses and re-forms elsewhere (orange and yellow) when it crosses its previous path (blue), presumably due to local food depletion. B) One-hour fluorescent recordings of *npr-1* animals under our experimental conditions consist of reproducible temporal dynamics encompassing three phases: transient (animals move about the lawn and start to form clusters), aggregation (clusters largely remain stable with individuals entering and exiting), and swarming (worms move across the lawn in persistent clusters). Percentage of in-cluster worms remain largely consistent throughout the latter two phases, except that clusters remain in place during the aggregation phase and become dynamic during the swarming phase. The average duration of each phase derived from *npr-1* experiments are applied to N2 data to maintain temporal consistency, even though N2 does not exhibit aggregation or swarming. Subsequent quantitative analyses for both strains were restricted to using the data from the aggregation phase, in order to reveal the mechanisms necessary for producing aggregation.

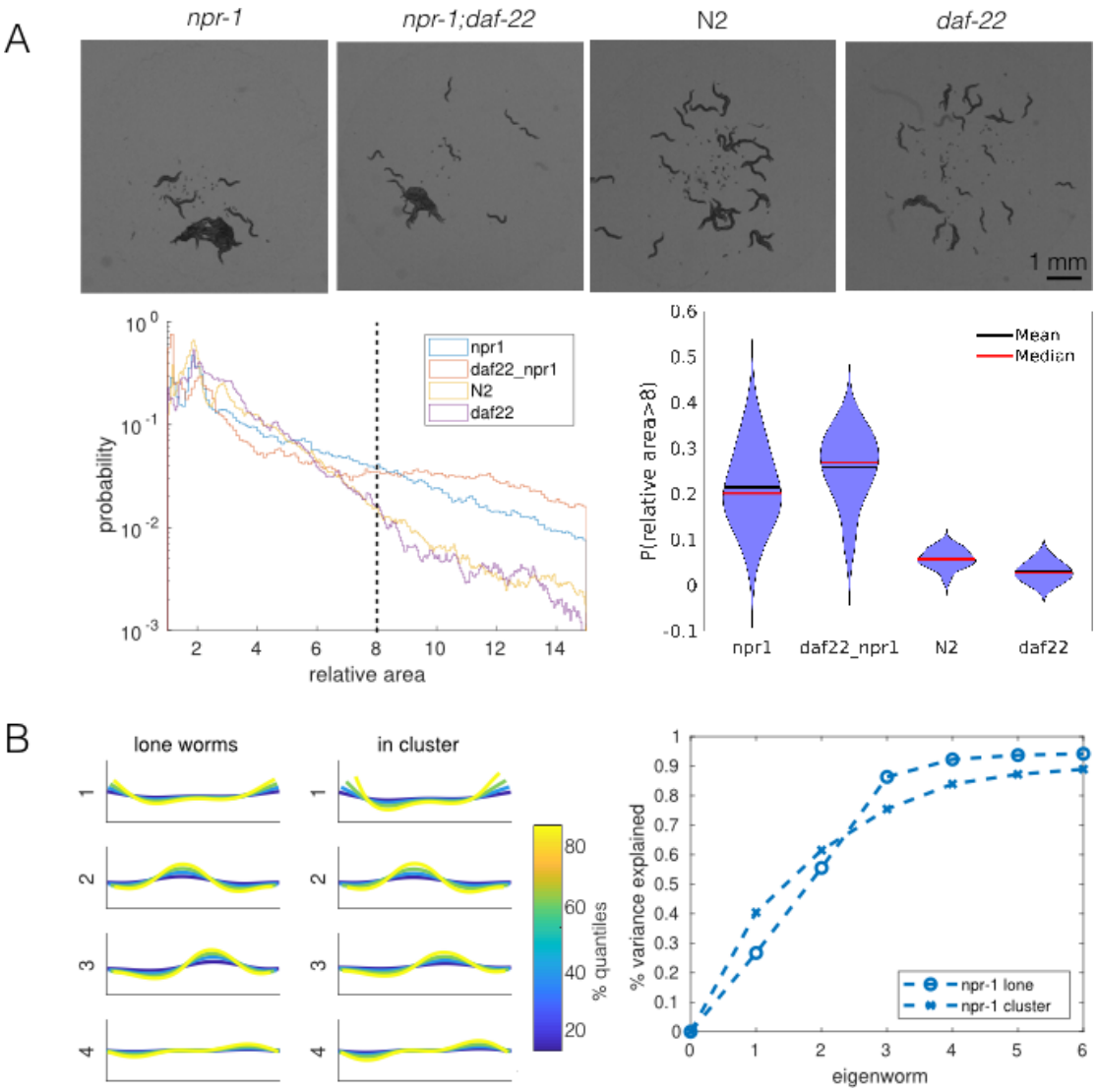

Supplementary Figure S2. Pheromones and shape changes appear unimportant for aggregation. A) *npr-1* and N2 animals with pheromones removed by a *daf-22* mutation aggregate to similar levels to their pheromone-intact counterparts. Top row: snapshots of 40 worms from each strain behaving on a thin, uniform lawn. Bottom left: quantification of average cluster area relative to corresponding feature of single worms, shown for each strain; dashed line shows the cut-off values used to generate the violin plot on the bottom right. Bottom right: probability of having a relative cluster area above the threshold values indicated by corresponding dashed lines on the bottom left. Blob area were extracted as tracking features. For each recording, a random sample (without replacement) of 500 single worms was used to calculate single-worm mean area, which was used to normalize multi-worm cluster areas from that recording. Relative cluster area values for each strain were pooled across recording replicates, and histograms were created with a bin width of 0.5. B) Shape analysis for lone and in-cluster *npr-1* worms. Left two panels: first four eigenworms (Stephens et al., 2008) plotted in real space for lone worms and in-cluster worms. Right: variance explained as a function of the number of eigenworms. Eigenworms are based on common reference (Brown et al., 2013) set for both strains and worm categories.

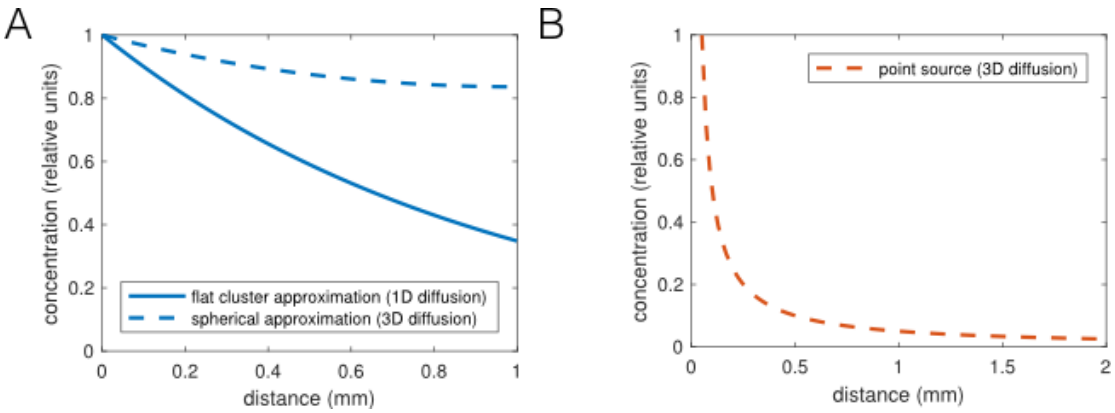

Supplementary Figure S3. Oxygen consumption-diffusion calculations predict shallow O_2 concentration gradients. A) Plot of feasible oxygen gradients inside worm aggregates. The oxygen concentration decays with length constant $\sqrt{D/\mu} \approx 1\,\mathrm{mm}$, with diffusion constant $D \approx 2.1\times10^{-5}\ \frac{\mathrm{cm}^2}{\mathrm{s}}$ (in water) and oxygen consumption rate $\mu \approx 0.14\ \mathrm{min}^{-1}$ (estimated as an upper bound for 200 pl/min (Shoyama, Shimizu, & Suda, 2009; Suda, Shouyama, Yasuda, & Ishii, 2005) at 21% oxygen and 8000 pl worm volume). The thinnest dimension of a cluster is relevant for diffusion, which is its thickness. We can approximate the cluster geometry either as flat, which results in a 1D diffusion gradient (solid line), or as hemispherical, which we approximate by spherically symmetric diffusion in 3D (dashed line). In either case the reaction-diffusion equation $\frac{\partial c}{\partial t} = D\nabla^2 c - \mu c$ was solved at steady state. B) Gradient of diffusible, non-degrading signal, e.g. CO_2, outside a point source. Without decay, this problem is equivalent to calculating the potential around a point charge, and the concentration would be $c = \frac{\lambda}{4\pi D r}$, in 3D, where λ is the production rate times the volume of a worm, 0.14/min (equal and opposite to the O_2 consumption, based on mass conservation). A point source represents the contribution of a short section of a worm, and the contributions of many worms in an aggregate would integrate to give an approximately logarithmic gradient of signal outside the aggregate.

Supplementary Movie Captions

Supplementary Movie S1. Sample movie showing *npr-1* collective feeding dynamics.

Supplementary Movie S2. A single event showing switch from high to low motility state prior to cluster entry. The red worm at the bottom (arrow) decreases speed before entering a cluster. Inset: midbody absolute speed of that individual with respect to time 0 as the point of the head entering a cluster; open blue circle shows the current speed matched to the movie frame.

Supplementary Movie S3. A single event showing switch from low to high motility state prior to cluster exit. The red worm increases speed before exiting a cluster. Inset: midbody absolute speed of that individual with respect to time 0 as the point of the head exiting a cluster; open blue circle shows the current speed matched to the movie frame.

Supplementary Movie S4. Sample extended model simulation describing *npr-1* mutants.

Supplementary Movie S5. Sample extended model simulation describing N2.

Supplementary Movie S6. Sample swarming simulation describing *npr-1* mutants.

Supplementary Methods

1 Agent-based simulations

We aim to create a model of worm locomotion and interaction that recapitulates aggregation and sweeping behaviour. Many mechanical models of worm locomotion exist in the literature, but we aim for a simpler representation of each individual worm, so that computationally inexpensive simulations of tens to hundreds of worms allow rapid hypothesis exploration and testing.

1.1 SPP worm model

Each agent is represented by M nodes connected linearly by $M-1$ segments. Each node moves as a self-propelled particle with a preferred speed v. At each time-step, the direction of movement is updated based on phenomenological forces representing active movement, interactions with other worms, and constrains to ensure the worm does not extend in length or bend excessively. Nodes follow forces in the over-damped regime, $\mathbf{v} \sim \mathbf{F}$, with periodic boundary conditions.

The code for model simulations is available at `github.com/ljschumacher/sworm-model`.

1.1.1 Self-propelled movement

To mimic a worm's persistent movement with directional changes over time, we add a stochastic contribution to the head node's movement, given by $\phi_1^{t+1} = \phi_1^t + \eta\xi$, where η is the noise strength, and ξ is a normally distributed random variable.

For the nodes following the head node, the direction of movement is given by the tangent vector towards the next node. For node i, the tangent vector is calculated as $\mathbf{s}_i = [(\mathbf{x}_i - \mathbf{x}_{i+1}) + (\mathbf{x}_{i-1} - \mathbf{x}_i)]/2$, i.e., the average between the direction towards the previous node and the direction from the next node. The motile force is then given by $\mathbf{F}_{m_i}^{t+1} = v\mathbf{s}_i$.

After forces have been applied and the nodes' positions updated, the headings are updated to reflect the direction of the displacement for calculating the movement in the next time step.

1.1.2 Taxis

To investigate the effect of taxis in our simulations, we treat the movement of the head node as a self-attracting walk with respect to other worm's nodes within an interaction radius R_t [see Hannezo *et al.*, 2017, SI]. This was implemented as an additional term $f_h\mathbf{p_h}$ added to the motile force that affects its direction as well as its the magnitude (reflecting additive contribution from multiple neighbouring worms). The parameter f_h controls the strength of taxis per other worm. The taxis force is additionally weighted by $1/r$ to reflect that nearby neighbours exert a stronger attraction, i.e. as if mediated by a non-degrading, diffusible factor, such as oxygen or CO2. The vector $\mathbf{p}_h$ is the sum of the directions towards other worms' nodes within the interaction radius, R_t, so that for worm k, the taxis contribution to the motile force is

$$f_h\mathbf{p}_{h_k} = \frac{f_h}{M}\sum_{r_{jk}<R_t}\frac{1}{r_{jk}}\frac{\mathbf{x}_j - \mathbf{x}_k}{|\mathbf{x}_j - \mathbf{x}_k|}. \tag{1}$$

The force is normalised by M to make it independent on the number of nodes in a worm.

1.1.3 Length constraints

To enforce approximately constant length of the worm, each node is connected by non-linear springs of rest length l_0 that resist an extension $\delta l = l - l_0$, where l is the length of the segment, with opposing force

$$\mathbf{F}_l = k_l\hat{\mathbf{l}}\frac{\delta l}{1-(\frac{\delta l}{l})^2}, \tag{2}$$

which points along the direction of the segment, $\hat{\mathbf{l}} = \mathbf{l}/l$.

1.1.4 Adhesion

To assess how aggregation is affected by a moderate adhesion (equal to both strains), such as could arise through liquid film forces [Gart *et al.*, 2011], we implemented a soft-core version of the Lennard-Jones potential. This gives rise to a force between any two nodes of *different* worms that is repulsive at short distances, attractive at intermediate distances, and zero at long distances. The force between two nodes

separated by $r < 3.75r_c$ (the cut-off was chosen to limit adhesive force to nearest neighbours) is given by a soft-core potential of a generalised Lennard-Jones form [Heyes, 2010]:

$$F_a = 8\frac{\epsilon_a}{\tilde{r}}\left[\left(\frac{\sigma_a}{\tilde{r}}\right)^2 - \frac{\sigma_a}{2\tilde{r}}\right], \tag{3}$$

where $\tilde{r} = 2\sigma_a/3 + r$. The parameter $\sigma_a = 2r_c$ was chosen so that the force becomes attractive at approximately above the node particle size, the exponent of the attractive term was chosen as -1 to reflect the $1/r$ dependence estimated for liquid film tension between two worms [Gart *et al.*, 2011], and the exponent of the repulsive term was set as -2 to win over the attractive term at short distances (to ensure volume exclusion).

1.1.5 Switching between slow and fast movement

Worms stochastically switch between movement at speeds v_0 and v_s with rates that depend on the local density of worms surrounding them. In the absence of other worms, the (Poisson) rates are k_{s0} to slow down from v_0 to v_s, and k_{f0} to speed up from v_s to v_0. These rates increase and decrease, respectively, with the number of neighbouring worm nodes within r_i of any node of the worm, such that

$$k_{\text{slow}} = k_{s0} + \frac{\mathrm{d}k_s}{\mathrm{d}\rho}, \tag{4}$$

where the linear dependence is chosen for simplicity, and $\frac{\mathrm{d}k_s}{\mathrm{d}\rho}$ is a free parameter, and

$$k_{\text{fast}} = k_{f0}\exp\left[-\frac{\mathrm{d}k_f}{\mathrm{d}\rho}\rho\right], \tag{5}$$

where the exponential decay was chosen to provide a lower bound of 0.

The local density ρ is estimated by counting the average number of other worms' nodes in a radius r_i around each node of the current worm.

$$\rho = \frac{1}{M}\sum_m^M\sum_n^N\sum_j^M \Theta(r_i - |r_m - r_{nj}|), \tag{6}$$

where $|r_m - r_{nj}|$ is the distance from the current node m to node j of worm m, Θ is the Heaviside step function (such that $\Theta(x) = 1$ if $x > 0$), and the sum over other worms skips the index of the current worm.

1.1.6 Reversals

To model reverse movement, we switch the direction of the nodes for the duration of the reversal, such that movement originates from the tail and the rest of the body follows. Reversals events are generated stochastically, with Poisson-rate r_{rev}, which depends on the local density via

$$r_{\text{rev}} = \frac{\mathrm{d}r}{\mathrm{d}\rho},, \tag{7}$$

where $\frac{\mathrm{d}r}{\mathrm{d}\rho}$ is a free parameter, and ρ is the local density as estimated above. Once a reversal rate has started, it lasts for $t_{\text{rev}} = 2$s, unless otherwise aborted (see Contact-dependent reversal events).

1.1.7 Contact-dependent reversal events

The rate of reversal events depends on whether the head and tail are in close proximity with other worms, being r_{rev} when only the head or tail is in close proximity to another worm, but not both, and zero otherwise. Head and tail nodes are specified as the first and last 10% of the nodes (rounded), respectively. Contact is registered if any other worm's nodes are within r_i of the head/tail nodes. If the worm is going forward and the tail is in contact, but the head is not, reversals occur with rate r_{rev}. If the worm is already reversing, and the tail is not in contact, but the head is, reversals stop with the same rate. If both or neither head and tail are in contact, no reversals occur (adding reversal rates as measured for freely moving worms did not qualitatively change the aggregation outcome of simulations).

1.1.8 Adaptive time-step

The time-step of simulations is chosen adaptively to maintain accuracy at higher forces. To achieve this the time-step scales inversely with the maximum magnitude of forces in the system, $\mathrm{d}T \sim \mathrm{d}T_0/\max(F_i)$. The precise scaling is chosen so that the node with the highest force acting on it moves no further in one time-step than 1/2 of the node radius.

1.2 Food depletion

For simulations with food depletion, food is initialised uniformly on a grid of size $L/(4r_c)$, where r_c is the node radius. Food concentration is set equal to 1 in arbitrary units. Before worm movement is calculated, food concentrations are checked. If the food is depleted at the grid-point closest to the head node of a worm, the worm moves at the faster speed v_0, regardless of other interactions (i.e. does not slow down and speeds up if previously slowed down). After worm movements, food is consumed in each grid-point by an amount r_{feed} per worm-head in that grid-point, with a minimum of zero food.

2 Parameter inference

2.1 Reduction to feasible parameter space

For the model 4 parameter model, with independent speed-switching rates and taxis interactions, we employ a strategy to exclude unfeasible regions of parameter space before running long simulations. Our reasoning is that interactions must be such that pairs of worms should not be stable for long times, and cluster of worms should be stable/unstable for *npr-1*/N2. We first sample parameters for pilot simulations from a regular grid, with 10^d samples, where d is the dimensionality of our parameter space. We then run simulations of worms starting as an overlapping pair, and assess whether they are within 1 mm of each other after 1 min of simulation (taking the median of 10 repeated simulations). If their separation is below the threshold, we discard the parameter sample. The remaining parameter samples are used to run simulations in which worms start out in a cluster (by confining their initial positions to a circle of 1.8 mm radius). These simulations are run for 300s, after which stability of the cluster is assessed by calculating the radius of gyration of the head-nodes of the worms. If the radius of gyration is above 3 mm (which corresponds approximately to worms being uniform distributed within a square of 7.5 mm side length), the cluster is deemed not stable and the parameter sample is discarded for *npr-1* simulations, and kept for N2 simulations. Both the pair- and cluster-stability thresholds are chosen conservatively to include rather than exclude potential parameter samples. Never the less, only a few percent of the initial parameter space remain as feasible for further inference. The remaining parameter samples are used to construct a prior distribution via kernel density estimation, i.e., centring a Gaussian distribution on each sample.

2.2 Summary statistics

We use the following summary statistics to quantify aggregation and compute the similarity between simulations and the experimental data:

1. The pair-correlation function compares the density of neighbours at a distance r to that expected under a uniform random distribution [Gurry *et al.*, 2009]:

$$S_1 = g(r) = \frac{A}{N(N-1)} \frac{\sum_i^N \sum_{j\neq i}^N \mathbf{1}_{ij}(r-a < r_{ij} \leq r)}{\pi(r^2-(r-a)^2)}, \tag{8}$$

   where r_{ij} is the distance between objects i and j, $A = L^2$ is the size of the simulation domain, chosen to match the estimated are of the food patch in experiments.

2. Hierarchical clustering (as implemented in MATLAB's `linkage`) quantifies the structure of a point pattern through agglomerative clustering. Each frame results in a dendrogram, or clustering tree. We summarize the distribution of these clustering trees through the overall distribution of branch lengths, S_2.

3. The standard deviation of the positions, $\sigma(\mathbf{x}) = \sqrt{\sigma(x)^2 + \sigma(y)^2}$, is a simple way to quantify the spread of points $\mathbf{x} = (x, y)$, which we average over time to give

$$S_3 = \langle \sigma(\mathbf{x}) \rangle_t. \tag{9}$$

4. The kurtosis or the sharpness of the distribution of positions,

$$S_4 = \langle \mathrm{Kurt}(\mathbf{x}) \rangle_t. \tag{10}$$

To compute these summary statistics, we randomly sample frames from experiments and simulations such that on average we have one frame every three seconds. To mimic the partial information about a worms position obtained from the pharynx-labelled imaging, we restricted the simulation analysis to the first 16% of the nodes (based on measurements of pharynx size relative to worm body length), from which centroid positions for each worm were obtained. We also computed the nematic order parameter [Weitz *et al.*, 2015], but found these to be low (≈ 0.2), and hence not an informative summary statistic of aggregation in our system.

2.2.1 Distance function

Before combining the summary statistics into a single distance function, we scale them for their overall magnitude and dimensionality as follows: We take the log-ratio of the summary statistics from experiments and simulations [Barnes *et al.*, 2012] to adjust both for the different scale of bins within distributions, and the different scales of summary statistics overall, such that such that each statistic is waited approximately equally, irrespective of its average magnitude.

We further note that higher dimensional summary statistics result in larger distance values, even if the difference in each dimension is equal to that of a lower dimensional statistic. We choose to normalise for this by dividing the distance by the square root of the dimensionality.

Thus, our distance function for summary statistic S_i with dimensionality D_i is given by

$$d_i = ||\log S_{i,\mathrm{obs}} - \log S_{i,\mathrm{sim}}||_2 / \sqrt{D_i}. \tag{11}$$

Supplementary Tables

Table 1: ***C. elegans* strains used in this study**

Name	Genotype	Source
DA609	*npr-1(ad609)X*	CGC
OMG2	*mIs12[myo-2p::GFP]II; npr-1(ad609)X*	Originated from CB5584 and DA609
OMG10	*mIs12[myo-2p::GFP]II*	Originated from CB5584; outcrossed 6x to CGC N2
OMG19	*rmIs349[myo3p::RFP]; npr-1(ad609)X*	Originated from AM1065 and DA609
OMG24	*rmIs349[myo3p::RFP]*	Originated from AM1065; outcrossed 6x to CGC N2
DR476	*daf-22(m130)II*	CGC
AX994	*daf-22(m130)II; npr-1(ad609)X*	Gift from Mario de Bono

Table 2: **Model parameters**

Parameter values listed were used as a default, unless otherwise stated. The following parameters were set to (or otherwise derived from) values as measured in the single worm behavioural database [Yemini *et al.*, 2013]: $v_0, r_c, L_w, \omega, \Delta_\psi, t_{\text{rev}}, v_s, k_{\text{slow}}(\rho = 0), k_{\text{fast}}(\rho = 0)$.

	Description	Value	Units
Motility:			
v_0	worm speed	0.33 (*npr-1*), 0.14 (N2)	mm/s
$\mathrm{d}T_0$	time-step	$r_c/v_0/8$	s
η	angular noise strength	0.05 (*npr-1*), 0.0326 (N2)	rad
Shape:			
r_c	node radius	0.035	mm
L_w	worm length	1.2	mm
M	number of segments	18	
l	segment length	$(L_w - 2 * r_c)/(M - 1)$	mm
k_l	linear spring stiffness	40 (rods)	[F]/[l]
Reversals:			
$\frac{\mathrm{d}r}{\mathrm{d}\rho}$	increase in reversal rate with density	free parameter	1/s
t_{rev}	reversal duration	2	s
r_i	interaction radius	$3r_c$	mm
Slowing:			
v_s	speed when moving slow	0.018 (*npr-1*), 0.014 (N2)	mm/s
$k_{\text{s0}}(\rho = 0)$	rate to switch to slow movement	1/275 (*npr-1*), 1/4 (N2)	1/s
$k_{\text{f0}}(\rho = 0)$	rate to switch to fast movement	1/0.9 (*npr-1*), 1/2.2 (N2)	1/s
$\mathrm{d}k/\mathrm{d}\rho$	increase in rate with density	free parameter	1/s
Taxis:			
f_{taxis}	strength of taxis force	free parameter	[F]
R_t	maximal interaction range for taxis	L	mm

Supplementary References

Barnes, C. P., Filippi, S., Stumpf, M. P. H. and Thorne, T. 2012. Considerate approaches to constructing summary statistics for ABC model selection. *Statistics and Computing*, **22**, 1181–1197. doi:10.1007/s11222-012-9335-7.

Gart, S., Vella, D. and Jung, S. 2011. The collective motion of nematodes in a thin liquid layer. *Soft Matter*, **7**, 2444. doi:10.1039/c0sm01236j.

Gurry, T., Kahramanogullari, O. and Endres, R. G. 2009. Biophysical Mechanism for Ras-Nanocluster Formation and Signaling in Plasma Membrane. *PLoS ONE*, **4**, e6148. doi:10.1371/journal.pone.0006148.

Hannezo, E., Scheele, C. L., Moad, M., Drogo, N., Heer, R., Sampogna, R. V., van Rheenen, J. and Simons, B. D. 2017. A Unifying Theory of Branching Morphogenesis. *Cell*, **171**, 242–255.e27. doi:10.1016/j.cell.2017.08.026.

Heyes, D. M. 2010. Thermodynamic stability of soft-core Lennard-Jones fluids and their mixtures. *Journal of Chemical Physics*, **132**, 064504. doi:10.1063/1.3319510.

Weitz, S., Deutsch, A. and Peruani, F. 2015. Self-propelled rods exhibit a phase-separated state characterized by the presence of active stresses and the ejection of polar clusters. *Physical Review E*, **92**, 1–9. doi:10.1103/PhysRevE.92.012322.

Yemini, E., Jucikas, T., Grundy, L. J., Brown, A. E. X. and Schafer, W. R. 2013. A database of Caenorhabditis elegans behavioral phenotypes. *Nature Methods*, **10**, 877–879. doi:10.1038/nmeth.2560.